atmosphere

MDPI

*Article*

# Urban Impacts on Convective Squall Lines over Chicago in the Warm Season—Part I: Observations of Multi-Scale Convective Evolution

**Michael L. Kaplan [1,*], S. M. Shajedul Karim [2,3] and Yuh-Lang Lin [2]**

[1] Division of Atmospheric Sciences, Desert Research Institute, Reno, NV 89512, USA
[2] Department of Physics, North Carolina A&T State University, Greensboro, NC 27411, USA; shajedul.87@gmail.com (S.M.S.K.); ylin@ncat.edu (Y.-L.L.)
[3] Center for Atmospheric Sciences, Hampton University, Hampton, VA 23669, USA
* Correspondence: michael.kaplan@dri.edu; Tel.: +1-775-300-8181

**Abstract:** In this study, our aim is to diagnose how two quasi-linear convective systems (QLCS) are organized so one can determine the possible role of the city of Chicago, IL, USA, in modifying convective precipitation systems. In this Part I of a two-part study, we employ large-scale analyses, radiosonde soundings, surface observations, and Doppler radar data to diagnose the precursor atmospheric circulations that organize the evolution of two mesoscale convective systems and compare those circulations to radar and precipitation. Several multi-scale processes are found that organize and modify convection over the Chicago metroplex. Two sequential quasi-linear convective systems (QLCS #1 and #2) were organized that propagated over Chicago, IL, USA, during an eight-hour period on 5–6 July 2018. The first squall line (QLCS #1) built from the southwest to the northeast while strengthening as it propagated over the city, and the second (QLCS #2) propagated southeastwards and weakened as it passed over the city in association with a polar cold front. The weak upper-level divergence associated with a diffluent flow poleward of an expansive ridge built over and strengthened a low-level trough and confluence zone, triggering QLCS #1. Convective downdrafts from QLCS #1 produced a cold pool that interacted with multiple confluent low-level jets surrounding and focused on the metroplex urban heat island, thus advecting the convection poleward over the metroplex. The heaviest precipitation occurred just south-southeast of Midway Airport, Chicago. Subsequently, a polar cold front propagated into the metroplex, which triggered QLCS #2. However, the descending air above it under the polar jet and residual cold pool from QLCS #1 rapidly dissipated the cold frontal convection. This represents a case study where very active convection built over the metroplex and was likely modified by it, as evidenced in numerical simulations to be described in Part II.

**Keywords:** convection; mesoscale; lake-breeze; jets; convergence; heating; urban



Academic Editor: Tomeu Rigo

Received: 1 February 2025
Revised: 2 March 2025
Accepted: 4 March 2025
Published: 6 March 2025

**Citation:** Kaplan, M.L.; Karim, S.M.S.; Lin, Y.-L. Urban Impacts on Convective Squall Lines over Chicago in the Warm Season—Part I: Observations of Multi-Scale Convective Evolution. *Atmosphere* **2025**, *16*, 306. https://doi.org/10.3390/atmos16030306



## 1. Introduction

Numerous simulations and observational analysis have been performed to diagnose the role of cities on precipitation systems. Since the pioneering studies of [1–3], the METropolitan Meteorological EXperiment (METROMEX) was held during 1971–1972 in St. Louis, MO., USA [4,5], and additional important urban studies conducted over cities such as Atlanta, Indianapolis, New York, and Dallas, (e.g., [6–11]), there has been a growing interest in and numerous studies of rainfall enhancement and/or redistribution by urban

areas. As noted in [12], most existing studies highlight three main pathways of urban rainfall modification: (1) urban heat island (UHI) (e.g., [7,13–20]), (2) the urban canopy effect (e.g., [21–23]), and (3) urban aerosols as cloud condensation nuclei (e.g., [24–27]). These studies differ substantially in terms of creating consistent signals of rainfall impacts caused by urbanization. Thus, extensive research is required to assess the urban forcing of rainfall patterns and the intensity impacts by urbanization. It is simply not clear from the literature whether varying urban forcing functions and/or varying synoptic circulation signals dominate urban impact responses during specific precipitation events.

One signal that does emerge with some consistency, however, is that weaker synoptic forcing allows the UHI to dominate, while the drag and blocking effects of buildings are more dominant in stronger synoptic flow regimes. Hence, these differences in physical forcing are differentiating primarily thermal from mechanical effects caused by the urban environment. The fundamental result of these forcing differences is that splitting and downstream effects of convective cellular motions are more typically forced by drag effects and increased downtown as well as downstream precipitation by the UHI, although these differences are far from universally true. As one of the numerous examples of urban impacts on precipitation, in an extremely comprehensive radar-based observational and modeling study by [22], it was found that more than 60% of storms changed structure over the Indianapolis area as compared with only 25% over the rural regions. Furthermore, daytime convection was most likely to be affected, with 71% of storms changing structure as compared with only 42% at night. Analysis of radar imagery indicated that storms split closer to the upwind urban region and merge again downwind. In this study, a larger portion of small storms (areal coverage = 50–200 $km^2$) and large storms (areal coverage > 1500 $km^2$) were found downwind of the urban region, whereas midsized storms (areal coverage = 200–1500 $km^2$) dominated the upwind region. Modeling sensitivity studies indicated that removing the Indianapolis urban region caused distinct differences in the regional convergence and convection as well as in simulated base reflectivity, surface energy balance (through sensible heat flux, latent heat flux, and virtual potential temperature changes), and boundary layer structure. The study results indicated that the urban area has a strong climatological influence on regional thunderstorms.

In a broader study, Ref. [28] examined the relationship between rainfall characteristics and urbanization over the eastern United States by analyzing four datasets: daily rainfall in 4593 surface stations over the last 50 years (1958–2008), a high-resolution gridded rainfall product, reanalysis wind data, and a proxy for urban land use (gridded human population data). Results indicate that summer monthly rainfall amounts show an increasing trend in urbanized regions. The frequency of heavy rainfall events has a potential positive bias toward urbanized regions. Most notably, consistent with case studies for individual cities, the climatology of rainfall amounts downwind of urban–rural boundaries shows a significant increasing trend. Ref. [28] showed that heavy (90th percentile) and extreme (99.5th percentile) rainfall events indicate decreasing trends of heavy rainfall events and a possible increasing trend for extreme rainfall event frequency over urban areas. Results indicate that the impact of urbanization is more pronounced in the northeastern and midwestern United States, with an increase in rainfall amounts. In contrast, the southeastern United States showed a slight decrease in rainfall amounts and heavy rainfall event frequencies. Results suggest that the urbanization signature is becoming detectable in rainfall climatology as an anthropogenic influence affecting regional precipitation; however, extracting this signature is not straightforward and requires eliminating other dynamical confounding feedback.

There has recently been an increased number of studies focusing on urban impacts on precipitation in Asian cities. Ref. [27] found from simulation studies in Beijing that convection often bifurcates in the windward periphery of the metroplex, producing more

rainfall on both sides of the city. The convergent response to the UHI increases rainfall in the peripheral regions. Ref. [16], employing an observational climatological analysis, found a precipitation maximum over downtown Beijing and downwind of the city. Simulations indicated a splitting of only the strongest storms around the city. Ref. [12] emphasized that, downwind of Nanjing, there was a general pattern of rainfall maxima but that was highly divergent depending upon the synoptic conditions, with extreme dependency on the environmental circulation. Ref. [29], in a literature review of many aspects of urban forcing, emphasized the lack of unanimity results in the effects of cities on precipitation. Ref. [10] investigated the urbanization-induced summer rainfall changes in the Yangtze River Delta by analyzing long-term observations and numerical simulations. The observation-based analysis showed that long-term urbanization increased the region's summer rainfall, particularly through the intensification of heavy rainfall, which is noted as the urban rain island (URI) effect. A series of numerical sensitivity experiments with three historical land use and land cover scenarios (1990, 2000, and 2010) were designed to further illustrate the impact of urbanization on rainfall. The observed URI effect was well reproduced by the numerical simulations, and on average, urban expansion during 1990–2010 increased summer rainfall over urban areas by 51.91 mm. The URI effect slightly weakened in the late stage of urbanization (2000–2010) compared to the early stage (1990–2000). They concluded that the strengthening of precipitation-inhibiting effects during the late period offset the precipitation-enhancing effects, which led to the weakening of the URI effect.

Additionally, urban forcing can be strongly influenced by local water bodies that produce lake or sea breezes. Ref. [30] demonstrated with observational data the complex impacts the Chicago UHI had on the Lake Michigan lake breeze front. Ref. [31], employing an idealized numerical model that diagnosed fine scale vortical and streak patterns, found that an idealized lake breeze front developed when it interacted with an urban convective boundary layer. This led to substantial impacts on urban turbulence kinetic energy and microscale wind patterns.

In our study, we focus on the multi-scale complex interactions among the Chicago UHI, Lake Michigan, and two propagating quasi-linear convective systems (QLCS). We will diagnose the impact of the city-scale urban canopy on the organization and propagation of the QLCS. In this manuscript, Part I, we employ multi-scale observations to clearly describe the organization and evolution of two QLCS that propagate over and were likely modified by the Chicago metroplex. This first manuscript provides proof of the environmental organization and control of convective systems. In Part II, we will focus on their motion and rainfall distribution/evolution modified by the detailed urban canopy as compared to a simple land use representation. The goal will be to determine how the UHI modifies the evolution of the observed convective systems and their surrounding environment. We will, in Part II, employ high-resolution Weather Research and Forecasting–Advanced Research Weather Model (WRF-ARW) and Weather Research and Forecasting–Urban Canopy Model (WRF-UCM) simulations, both of which will be compared to and validated against the observations in Part I, i.e., surface, upper-air, Doppler rainfall, and Doppler reflectivity data over the Chicago metroplex during 5–6 July 2018. Subtle differences between the simulations will be the focal point of Part II. In Section 2 of this manuscript, Part I, we will describe the observations employed in the analysis. Section 3 will focus exclusively on organizing synoptic to meso-$\alpha$ scale circulations. Section 4 will focus on meso-$\alpha/\beta$ scale processes. Section 5 will focus on meso-$\gamma$ scale processes almost exclusively from the Next Generation Weather Radar (NEXRAD) and surface datasets. Section 6 will summarize the results.

## 2. Observational Data Employed and Area of Study

The methodology employed involved detailed multi-scale analyses of observational datasets. Observed upper-air Rapid Update Cycle (RUC) analyses fields were derived from the NOAA Storm Prediction Center Mesoscale Analyses Archives [32], observed soundings from the University of Wyoming Sounding Archive [33], observed surface meteograms and supporting observational analyses from the Plymouth State Weather Center Surface Data Archives [34], and Doppler radar reflectivity and precipitation from the NOAA Next Generation Doppler Weather Radar Archive [35]. All datasets used in this study are summarized in Table 1.

**Table 1.** Different types of datasets used for this study.

| Analysis Type | Data Provider | Major Meteorological Variables |
|---|---|---|
| Upper-air Rapid Update Cycle (RUC) | NOAA SPC | Potential Vorticity, Precipitable Water, Velocity Divergence and Convergence, Convective Available Potential Energy (CAPE), Most Unstable CAPE (MUCAPE), Surface-based CAPE (SBCAPE), Convective Inhibition (CIN), Omega, etc. |
| Upper-air Sounding | University of Wyoming | Atmospheric Thermodynamic Sounding, including temperature, humidity, pressure, and wind profiles |
| Surface Observation | Plymouth State Weather Center-Surface Data Archives | Temperature, Mean Sea Level Pressure (MSLP), streamlines |
| Surface Meteogram | Plymouth State Weather Center | Time variation of temperature, MSLP, dew point, winds |
| Level III Doppler radar | NOAA NEXRAD | Reflectivity and precipitation |

RUC data were utilized to analyze the larger scale organizing upper-air ridges and troughs, jets, fronts, moisture, and static stability fields. Soundings were employed to diagnose the convective potential. Surface observations to map out the motion and evolution of thermodynamical variables during moist convection. Radar data explicitly represented the development and dissipation of moist convection. Numerous meteorological variables were considered to explain the multi-scale process that organizes this closely linked convective squall line. Standard variables included temperature in Celsius, mean sea level pressure in hectopascals, winds in m/s, and the height of a constant pressure surface in m. Derived fields included the velocity divergence/convergence in 1/s indicating the horizontal gradients of wind velocity, precipitable water as a measure of the column integrated water vapor in g/kg, radar reflectivity of precipitation in decibels, dewpoint temperature indicating saturation conditions in Celsius, omega indicating upward and downward air motion in microbars/s, streamlines indicating lines tangent to airflow, and stability indices indicating upward buoyancy including MUCAPE, SBCAPE, mixed layer CAPE (MLCAPE), and CIN or the resistance to upward buoyancy.

Figure 1 describes the area of study, focusing on Chicago, IL, USA, and its adjacent states. For the analysis, we particularly focus more closely on the Chicago metroplex and its adjacent urban cities (rectangle box area), where urban impacts are more dominant. The evolution of meso-$\gamma$ radar and surface data over the Chicago metroplex, in response to the meso-$\alpha/\beta$ scale processes upstream, is organized by the synoptic-meso-$\alpha$ scale circulations.

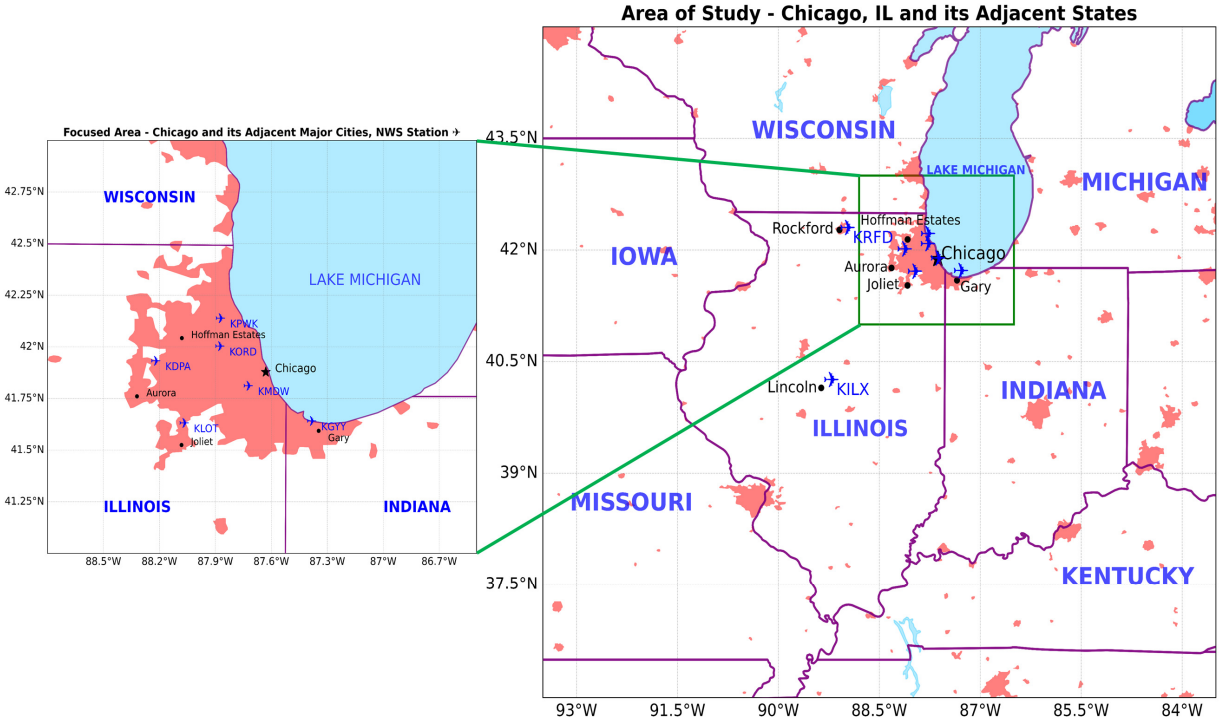


**Figure 1.** Study area focuses on Chicago, IL, USA, and its adjacent states. For analysis, focus is mainly on Chicago metropolitan region, annotated by a green rectangle box. Analysis of meso-$\gamma$ scale observations included National Weather Service (NWS) stations, namely Romeoville, IL (KLOT), Midway Airport (KMDW), O'Hare Airport (KORD), Wheeling, IL (KPWK), DuPage County, IL (KDPA), Rockford Airport (KRFD), Lincoln, IL (KILX), and Gary, IN (KGYY). Shaded red color indicates urban area. Black dots indicate major adjacent urban cities.

## 3. Key Synoptic-Meso-$\alpha$ Scale Circulations

This case study epitomizes relatively weak summertime synoptic-scale forcing over the mid-continental U.S. but with extensive complexity in convective organization and evolution. Synoptic-scale features depicted in Figure 2 are evident in the RUC analyses of 12-hourly mid-upper-tropospheric isobaric potential vorticity (PV) and upper tropospheric streamline fields during the precursor ~36–6-h period prior to convective evolution over Chicago. These two dominant features are (1) the expansive ridge which retrogresses from the mid-Atlantic to Mississippi River Valley as it elongates southwestwards to northwestern Mexico and (2) the strong trough and PV maximum in the cyclonic shear zone of the polar jet that propagates from the northern Rockies to western Ontario (Figure 2b–d). High pressure ridges (anticyclones) are regions of low inertial stability but significant static stability with low numerical values of isobaric PV, which is equal to the product of absolute vertical vorticity and static stability, while troughs (cyclonic regions) are regions of high inertial stability and low static stability with large values of isobaric PV. By 1200 UTC 5 July 2018 (hereafter following the format: 12007/5), northeastern Illinois and northern Indiana were both within the diffluent anticyclonic shear zone in the mid-upper tropospheric flow poleward of the elongated ridge. Difluence is indicated by the spreading streamlines parallel to the wind flow, where the flow diverges aloft. Even at this scale, there is an indication of a sub-synoptic split in the flow in this diffluent area over northern Illinois in Figure 2d (see red arrow), with a zonal (westerly) streamline located northwestward of an anticyclonic streamline prior to the organization of convection in this region. This reflects the significant stretching and elongation of the ridge over the 36 h prior to 12007/5, which is evident in the sequence in Figure 2b–d as it extended across the entire U.S. into northwestern Mexico.

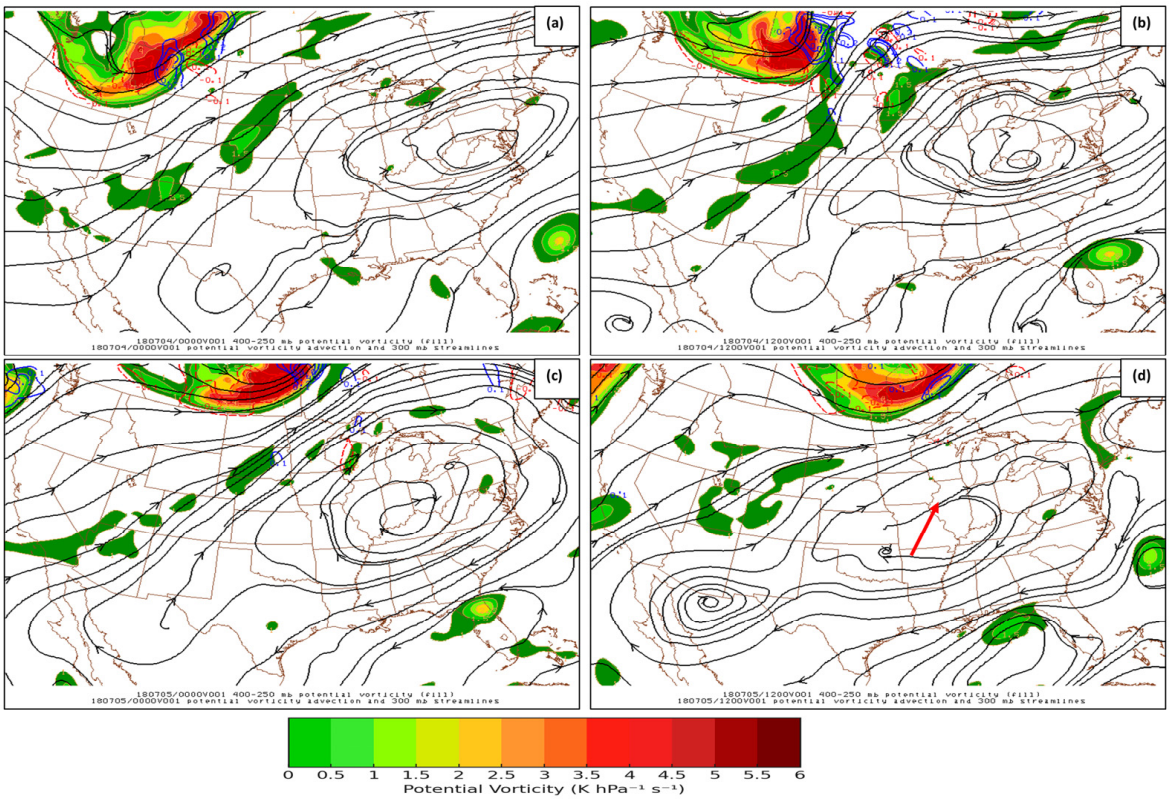


**Figure 2.** RUC one-hour forecasts of 300 hPa streamlines (black solid arrows), 400–250 hPa isobaric potential vorticity (IPV; color fill, K $hPa^{-1}$ $s^{-1}$), and IPV advection (positive blue solid, negative red dashed) valid at (**a**) 00007/4, (**b**) 12007/4, (**c**) 00007/5, and (**d**) 12007/5. Red arrow in (**d**) indicates the area of split streamlines south of Chicago, IL, USA.

The dominance of the poleward trough and extensive southwestward-building and elongated ridge are further indicated by those circulations' impacts on moisture transport over the same period depicted in Figure 3. There are three dominant zones of 850 hPa moisture transport that strongly control the column precipitable water (total column integrated water vapor) across the central and eastern regions of the U.S.: (1) the surge of moisture southeast of the eastward-propagating poleward trough into the Northern Plains consistent with a strong low-level southwesterly jet (Figure 3a,b), (2) the westward surge of moisture across the Mid-South on the equatorward side of the ridge (Figure 3c,d), and (3) the eastward surge of moisture across the upper Mississippi River Valley and ultimately into Illinois and Indiana on the poleward side of the ridge (red oval shape; Figure 3e–h). The later period confluence or convergence of moisture between the anticyclonic turning low-level jet southeast of the trough and the eastward flow on the poleward side of the ridge maintains copious low-level moisture in place over Illinois and Indiana under the diffluent sub-synoptic flow aloft (Figure 3c–h). The concentration of copious low-level moisture over Illinois relative to regions east and west, i.e., >2 inches column precipitable water in Figure 3e,g, is apparent from the local maximum of precipitable water over this region at 00007/5 and 12007/5. Its significance in conjunction with 1–3 °C surface temperature increases at KLOT, KMDW, and KORD (as discussed later in Figure 11a–c) for the development of convection is reflected in the MLCAPE, MUCAPE, and SBCAPE magnitude change (an increase of several hundred J $kg^{-1}$) during 0900-12007/5 and the very significant SBCAPE > 2000 J $kg^{-1}$ in the KILX sounding at 12007/5 all in Figure 4a–d. These CAPE parameters are direct measures of convective energy and vary as a function of where air parcels' static stability varies in the column, i.e., within the planetary boundary well-mixed layer, most unstable layer, or at the surface, respectively. The KILX balloon sounding

(Figure 4d) indicates the significant planetary boundary layer (PBL) moisture with ⩾20 °C dew points over ~100 hPa in the lower PBL and a dry adiabatic lapse rate to ~850 hPa above a very warm early (0700 CDT) near-surface (~980 hPa) temperature approaching 30 °C at 12007/5. This combination of PBL heat and moisture is largely responsible for the KILX sounding having much more CAPE than all the other surrounding radiosonde balloons in Iowa, Wisconsin, Indiana, and Michigan at 12007/5.

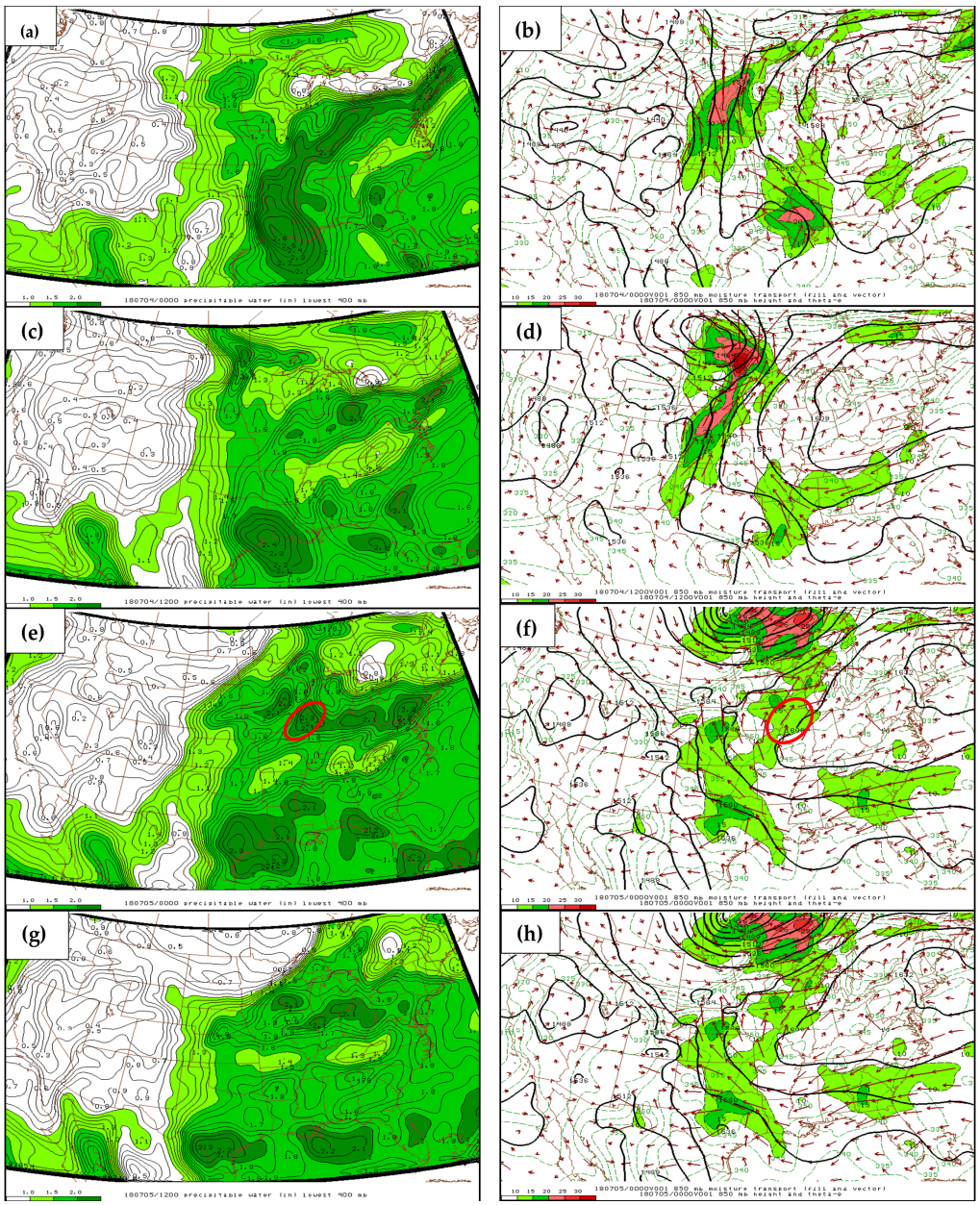


**Figure 3.** RUC one-hour forecasts of total column precipitable water (black solid < 1 inch, green fill > 1 inch), 850 hPa moisture transport (red vectors, color fill > 10 g kg$^{-1}$ s$^{-1}$), height (black solid, m), and equivalent potential temperature (green dashed, K), respectively valid at (**a**,**b**) 00007/4, (**c**,**d**) 12007/4, (**e**,**f**) 00007/5, and (**g**,**h**) 12007/5. Red oval-shaped area in (**e**,**f**) highlights eastward surge of moisture.

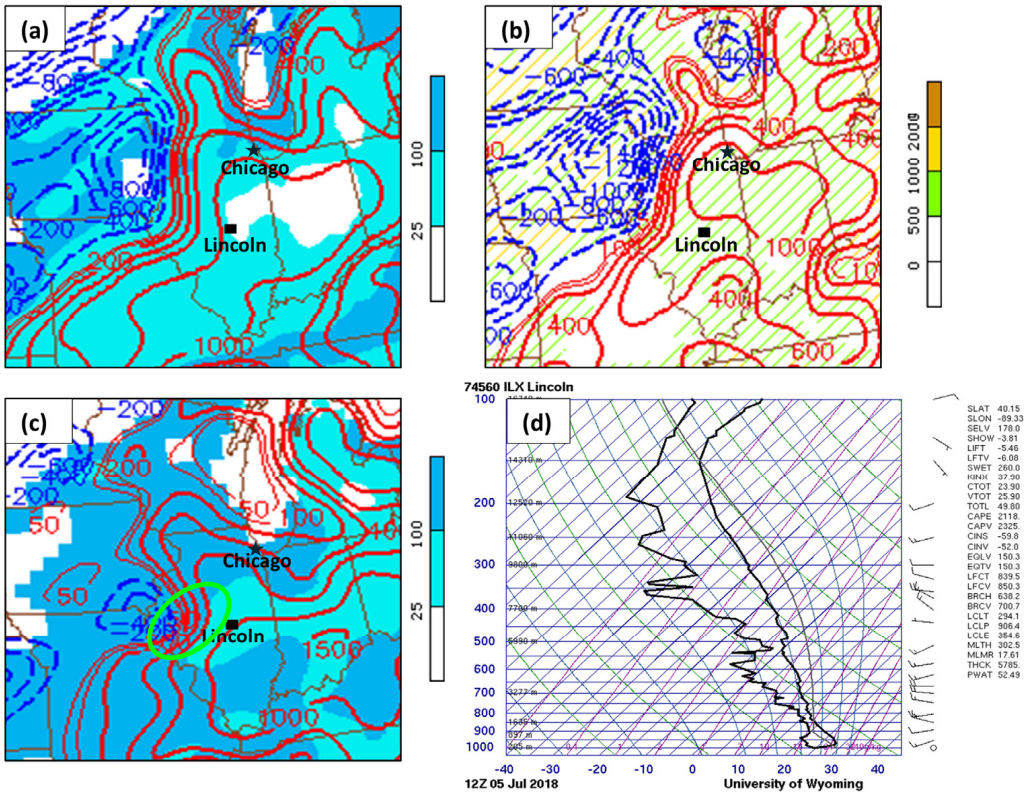


**Figure 4.** Zoomed in area of RUC analyses of (**a**,**c**) 3-h (0900–1200 UTC 5 July 2018) mixed layer CAPE, MUCAPE change, and SBCAPE change (thin red line for smaller values and thick red line for larger values in J kg$^{-1}$), CIN (convective inhibition = blue fill in J kg$^{-1}$) and in (**b**) MUCAPE change, LCL height (parcel saturation level = green hatched in m AGL) and (**d**) Lincoln, Illinois (KILX) sounding valid at 12007/5. Star indicates location of Chicago, IL, USA, and square indicates location of Lincoln, IL, USA. Green oval-shaped area in (**c**) highlights area of significant SBCAPE > 2000 J kg$^{-1}$ southwest of Chicago, IL, USA.

## 4. Meso-$\alpha$/$\beta$-Scale Organization of the Convective Environment

Figures 5–7 depict the observed deep mass adjustments during the period when the first line of convection initiated and began to propagate towards and through Chicago, peaked in intensity, followed shortly thereafter by weakening and the development of a shorter-lived second line as the polar front approached, which dissipated over the city. The mass adjustments are inferred from the diverging or splitting flow aloft relative to the converging low-level flow. Increasing divergence aloft and convergence in the PBL organize significant vertical motions (omega < 0). For clarity, when discussing the first and second lines of convection, see the organization of QLCS #1 in Figure 12a–g between 17007/5 and 18507/5 and the evolution of QLCS #2 in Figure 12l–o between 22007/5 and 00007/6, respectively. Between 12007/5 and 16007/5 (Figure 5a–c,g–i), 250 hPa velocity divergence, 850 hPa velocity convergence, and significant mid-tropospheric ascent over northwestern Indiana intensified in response to the growing diffluent and highly deformative flow poleward of the southwestern-building massive ridge aloft and well equatorward of the polar cold front, as shown earlier in Figure 2d with the aforementioned splitting of the streamlines just southeast of Chicago. Divergence aloft, low-level convergence, and ascending motion first built upstream (westwards from northern Indiana in Figure 5a–c,g–i) as denoted by the green fill and red lines defining the 250 hPa divergence and 850 hPa convergence in Figure 5a–c, as well as the magenta lines defining the mid-tropospheric (700–500 hPa) omega in Figure 5g–i, respectively, and then poleward through the region on the western and equatorward sides of Lake Michigan in Figures 5d–f and 5j–l, respectively,

between 18007/5 and 20007/5. Note in Figure 5d–f,j–l that once the 250 hPa divergence moved west of Lake Michigan after 1600 UTC, the upper-tropospheric (250 hPa) divergence and lower tropospheric (850 hPa) convergence were being modified by the diabatic (convective) heating as inferred from the aforementioned early radars in Figure 12a–g after 17007/5 for QLCS #1. This upscale growth of divergence aloft at 250 hPa and convergence at 850 hPa after 16007/5 is consistent with a mesoscale convective system to be described in the next subsection that began to redevelop and propagate from northwestern Indiana along the southwestern periphery of Lake Michigan and southwestwards from that location (in association with QLCS #1).

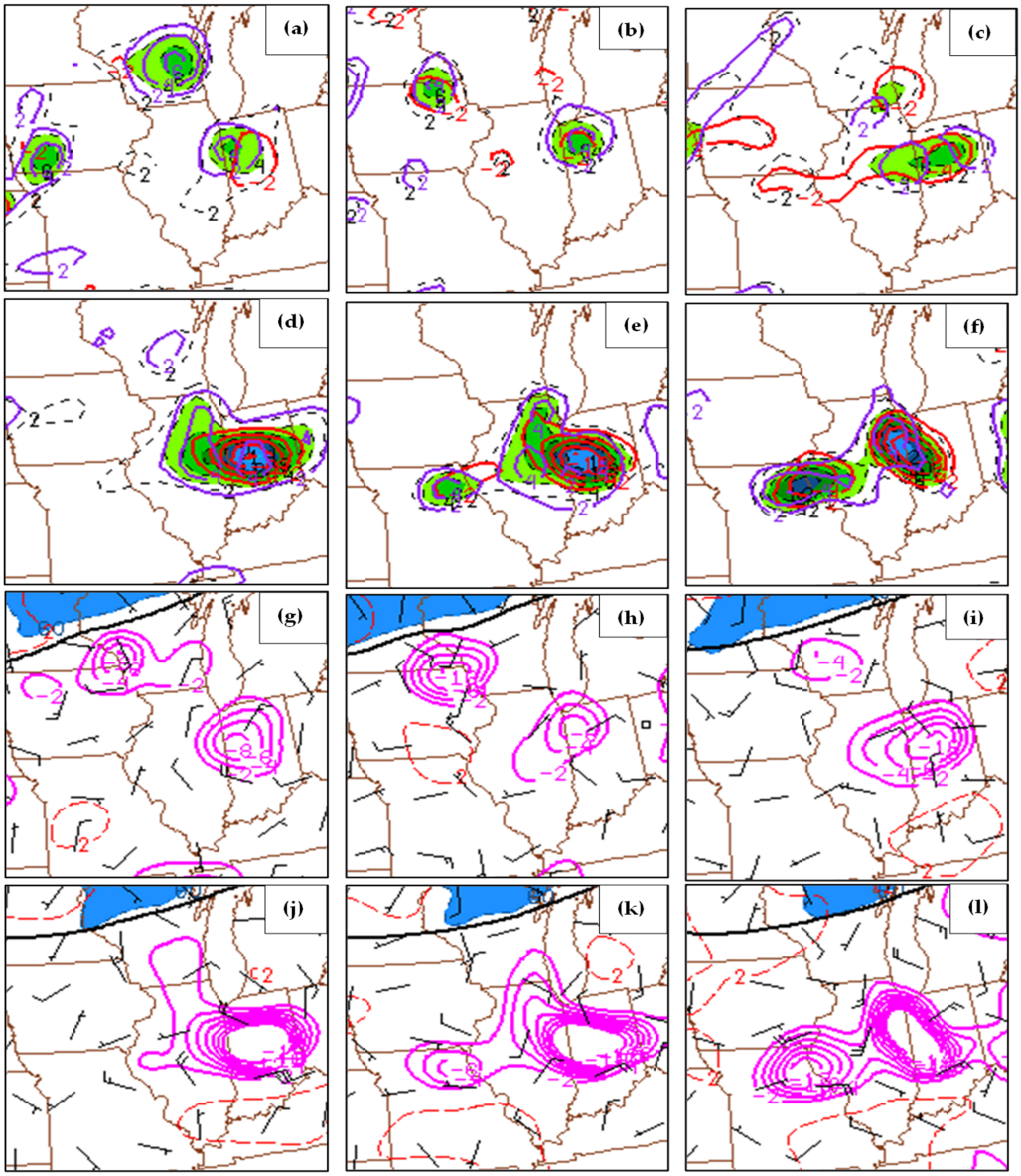


**Figure 5.** Zoomed in area of RUC analysis of 250 hPa velocity divergence (purple solid, $10^{-5}$ $s^{-1}$), 850 hPa velocity convergence (black or red dashed, $10^{-5}$ $s^{-1}$), and vertically differential velocity divergence (green or blue fill, $10^{-5}$ $s^{-1}$) valid at (**a**) 12007/5, (**b**) 14007/5, (**c**) 16007/5, (**d**) 18007/5, (**e**) 19007/5, and (**f**) 20007/5; and 300 hPa ageostrophic wind barbs (kt) and 700–500 hPa omega (magenta solid upward/red dashed downward, $\mu bs^{-1}$) valid at (**g**) 12007/5, (**h**) 14007/5, (**i**) 16007/5, (**j**) 18007/5, (**k**) 19007/5, and (**l**) 20007/5.

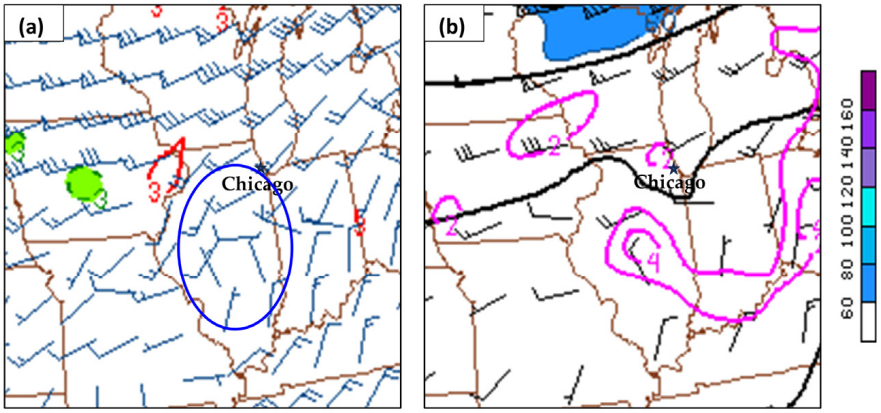


**Figure 6.** Zoomed in area of RUC analysis of (**a**) 250 hPa wind barbs (kt) and velocity tensor magnitude (red solid, $10^{-4}$ $s^{-1}$) and (**b**) 300 hPa wind barbs (kt), height (black solid, m), isotachs (color fill > 60 kt) and divergence (magenta solid, $10^{-4}$ $s^{-1}$) valid at 19007/5. Star indicates the location of Chicago, IL, USA. Blue circle in (**a**) highlights area of wind barb speed variation just southwest of Chicago, IL, USA.

Between 16007/5 and 18007/5, the convection built polewards into the southwestern suburbs of Chicago, consistent with the growth of 250 hPa velocity divergence, 850 hPa velocity convergence, and strong mid-tropospheric ascent west of Lake Michigan and extending into north-central Illinois. These mass adjustments wrapped around the northwest flank of the mid-upper tropospheric ridge shown in Figure 2 to be located over north-central Indiana and Illinois in Figure 5d,j at 18007/5. Nearly superposed divergence aloft, low-level convergence, and mid-tropospheric ascent can be seen in the two-hourly sequences in Figure 5.

By 1900 UTC, both the 250 hPa and 300 hPa fields in Figure 6 indicated a split in the southwesterly flow with an along-stream (southwest-northeast) velocity gradient in the anticyclonically-turning flow aloft over and adjacent to Chicago, as well as a sub-synoptic height minimum where the subgeostrophic vector was directed against the flow in Figure 5d,e,j,k at the same and earlier time periods. The mass field was adjusting, thus inhibiting the wind from achieving geostrophic balance where the pressure gradient force equally opposed the Coriolis force. This indicates that the mass outflow from strengthening convection over northwestern Indiana was enhancing the divergence by building a juxtaposed ridge and trough aloft at sub-synoptic scales of motion that eventually built over the city as that outflow strengthened along the southern and western Lake Michigan shore, consistent with the following studies [36–39].

By 2000 UTC, the vertically varying velocity divergence and mid-tropospheric ascent peak in magnitude over the metroplex in Figure 5f and Figure 5l, respectively. Figure 6a exemplifies this upscale convectively-forced outflow of mass or adjustment process as the lack of a velocity tensor (red isoline) in the 19007/5 250 hPa along-stream wind gradient near and over Chicago was consistent with a mesoscale convective outflow jetlet accelerating the flow downstream, i.e., strong stretching of the flow indicating outflow of mass aloft [36].

By 00007/6, the meso-$\alpha$/$\beta$ scale environment becomes considerably less favorable for moist convection, as can be seen in Figure 7a–f, leading to the dissipation of the convective line (QLCS#2) in Figure 12l–o between 22007/5 and 00007/6. Upper-tropospheric convergence and descent build over the region in concert with the approaching polar cold front and the sinking circulation on the anticyclonic flank of the polar jet. Dry air aloft overruns the low-level moisture, thus inhibiting convection, which is most noticeable when comparing the relative humidity at 925 hPa and 700 hPa in Figure 7a–d.

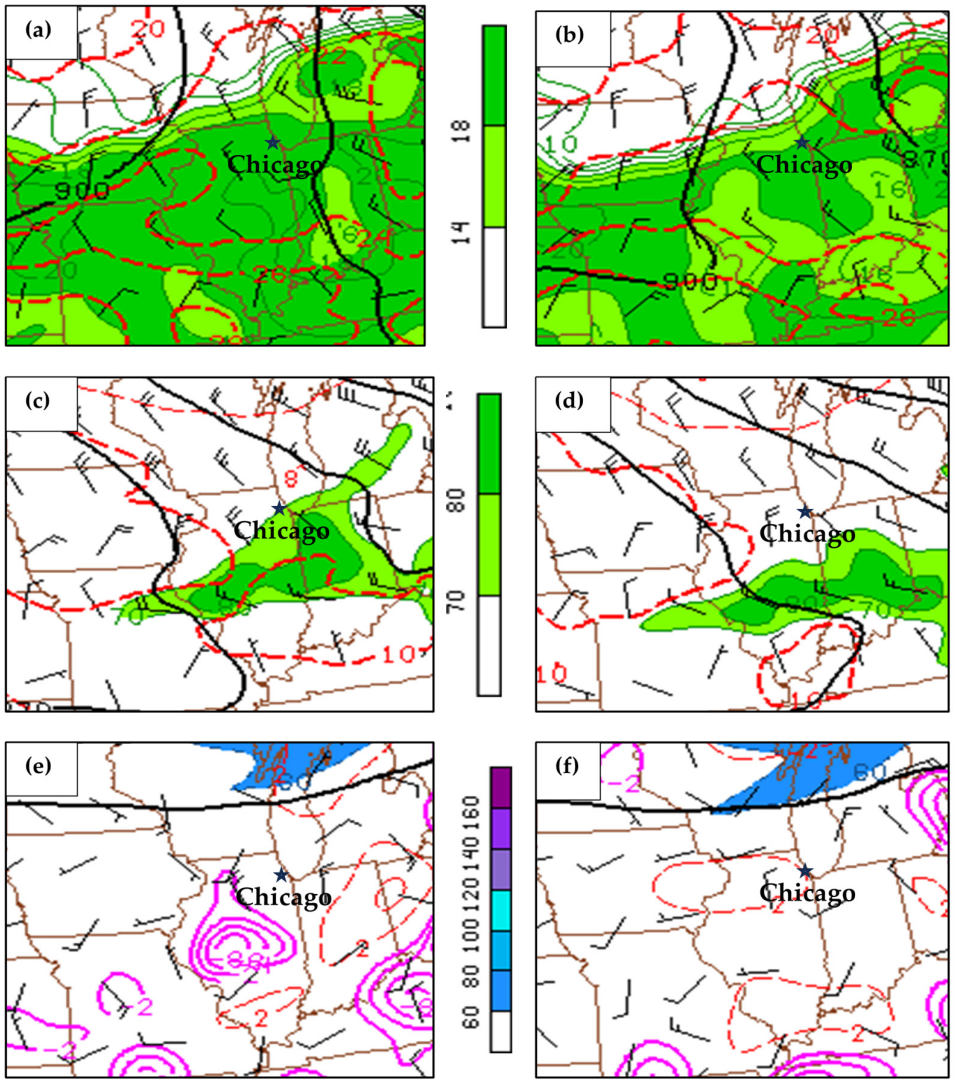


**Figure 7.** Zoomed in area of RUC analysis of (**a**,**b**) 925 hPa wind barbs (kt), height (black solid, m), isotachs (color fill > 60 kt), temperature (red dashed, °C), and dewpoint temperature (green solid, fill > 14 °C) valid at 00007/6 and 02007/6. (**c**,**d**) 700 hPa wind barbs (kt), height (solid black in m), mean relative humidity (green fill > 70%), and temperature (dotted red line in °C) valid at 00007/6 and 02007/6. (**e**,**f**) and 300 hPa ageostrophic wind barbs (kt), isotach (blue fill > 60 kt), and 700–500 hPa omega (magenta solid upward/red dashed downward, $\mu bs^{-1}$) valid at 00007/6 and 02007/6. Star indicates location of Chicago, IL, USA.

Early west-northwesterly flow and steady pressure observations along the southern and southwestern shore of Lake Michigan during 12007/5–15007/5 were soon replaced by three-hour pressure falls during 15007/5–18007/5, followed by three-hour rises during 18007/5–21007/5 in Figure 8a–c. This occurs as a confluence zone comprised of a large part of onshore Lake Michigan air entering into a mesoscale low-pressure (L) area southeast of the city (Figure 8b,e). Subsequently, that confluence zone propagated northwestwards, and then was replaced by a mesoscale high (H; Figure 8c), strong surface diffluence (Figure 8f), and strong poleward-directed outflow over Chicago, all during the period spanning 15007/5 through 21007/5 in Figure 8a–f. The meso-low was consistent with the mass flux divergence aloft depicted in Figure 5a–c over northwestern Indiana. As will be shown in the next subsection (Figure 12a–f), the explosive surface cooling and meso-low quickly followed by meso-high formation during the 1800–2100 UTC period reflects the rapid intensification of convection southwest of and over the Chicago metroplex most evident between 18007/5 and 19307/5. The MSLP and surface kinematics reflect the

transition from convection developing and intensifying from northwestern Indiana through the Chicago metroplex with QLCS #1 in Figure 12a–g. This convection occurs in between confluent surface flow reflecting an: (1) onshore wind component, (2) southeasterly wind component, and (3) north-northwesterly wind component southeast of, south of, and west of, respectively, surface convergence primarily into the region just southeast of Midway Airport (KMDW). This surface flow intensification was embedded within the persistent low-level meso-$\alpha/\beta$ scale pressure trough that is apparent from Figure 10c,d under the increasing northwest-propagating divergence aloft in Figure 5c at and just after 16007/5. This trough was located along a northeast–southwest axis straddling the metroplex, which is apparent from the MSLP and surface vorticity field in Figure 10c,d with an oscillating poleward–equatorward location in the surface streamline fields in the hours leading up to convective development over Chicago. While weak indications of that trough existed before convection, it strengthened between 16007/5 and 18007/5 under the diverging flow aloft accompanying the along-stream variation in wind depicted in Figure 6a,b between 300 and 250 hPa, as well as surface water vapor mixing ratio and SBCAPE increases (Figure 10a,b,e,f). Temperatures at KMDW and surrounding stations in Chicago (Figure 9) maximized at 18007/5~35 °C with nearby observations >32 °C over the city.

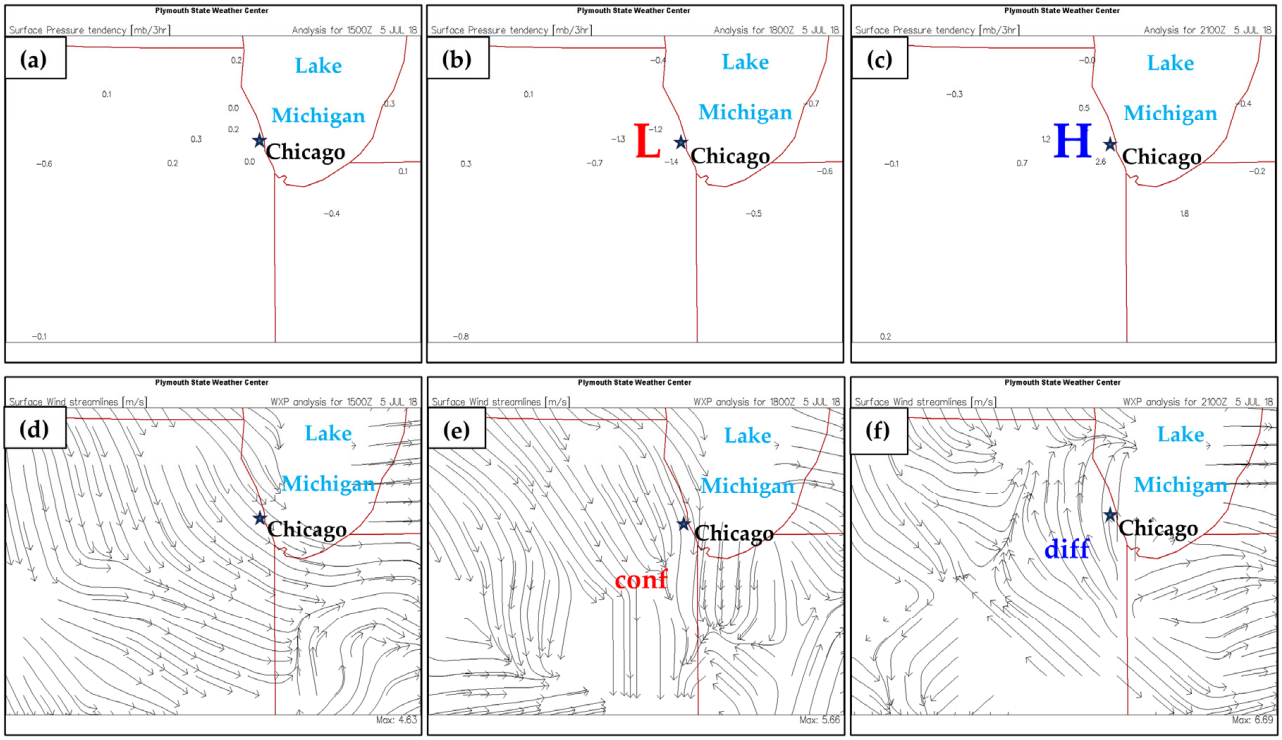


**Figure 8.** Mean sea level pressure (MSLP) tendency [hPa (3 $h^{-1}$)] observations valid at (**a**) 15007/5, (**b**) 18007/5, and (**c**) 21007/5. Surface streamline analyses are valid at (**d**) 15007/5, (**e**) 18007/5, and (**f**) 21007/5. L and H, just south-southwest of Chicago, signify meso-low and meso-high transitions, respectively, consistent with evolving surface confluence (conf) and difluence (diff) from northwestern Indiana to Chicago. Star indicates location of Chicago, IL, USA.

Figure 10 indicates temperature rose over the metroplex, and then fell 2 h later by more than 12 °C, reflecting the convective cooling and significant surface mass increases due to convective downdrafts within the aforementioned meso-high. By 21007/5, that meso-high accelerated the surface flow poleward and westward throughout most of the metroplex and generated very strong diffluent surface flow (Figure 9c,f).

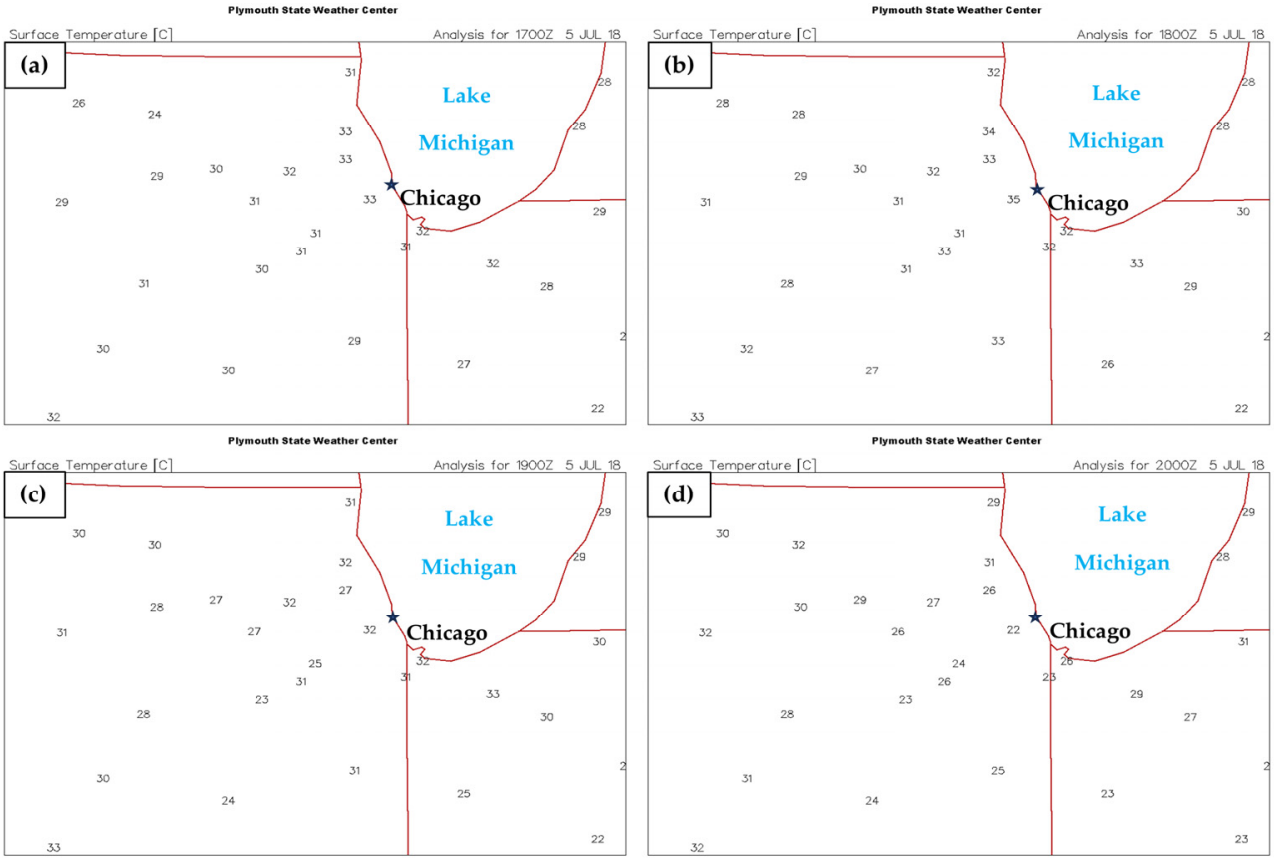


**Figure 9.** Surface temperature (°C) observations valid at (**a**) 17007/5, (**b**) 18007/5, (**c**) 19007/5, and (**d**) 20007/5. Star indicates location of Chicago, IL, USA.

The impact of the observed deep and surface mass and momentum adjustments and surface heating are reflected in the PBL moistening and building of large surface-based CAPE southeast of and over the Chicago metroplex in the pre-convective period prior to 18007/5. Figure 10a,b depicts that PBL moistening during 12007/5–14007/5 as the convergence of moisture into the surface trough (black contour; Figure 10c) strengthened. As the low levels warmed and moistened, very substantial SBCAPE, MUCAPE, and MLCAPE increased progressively towards Chicago and the Lake Michigan southwestern shoreline through 18007/5 in Figure 10e–g. This increase was later followed by sharp SBCAPE decreases through 22007/5 in Figure 10h. Consistent with the maximum temperature at 18007/5 at KMDW in Figure 9b, the SBCAPE maximum built over the same region until it weakened rapidly after 18007/5 in response to the explosive poleward growth of cooling and meso-high propagation through the city depicted in Figures 8–10. Shortly thereafter, the active redeveloping convection (Figure 12) in the northeast–southwest trough in Figure 10c,d consumed all the SBCAPE, as can be seen in Figure 10h. In the next subsection, we will demonstrate the observational linkage among these mesoscale features and detailed Doppler radar reflectivity and precipitation evolution.

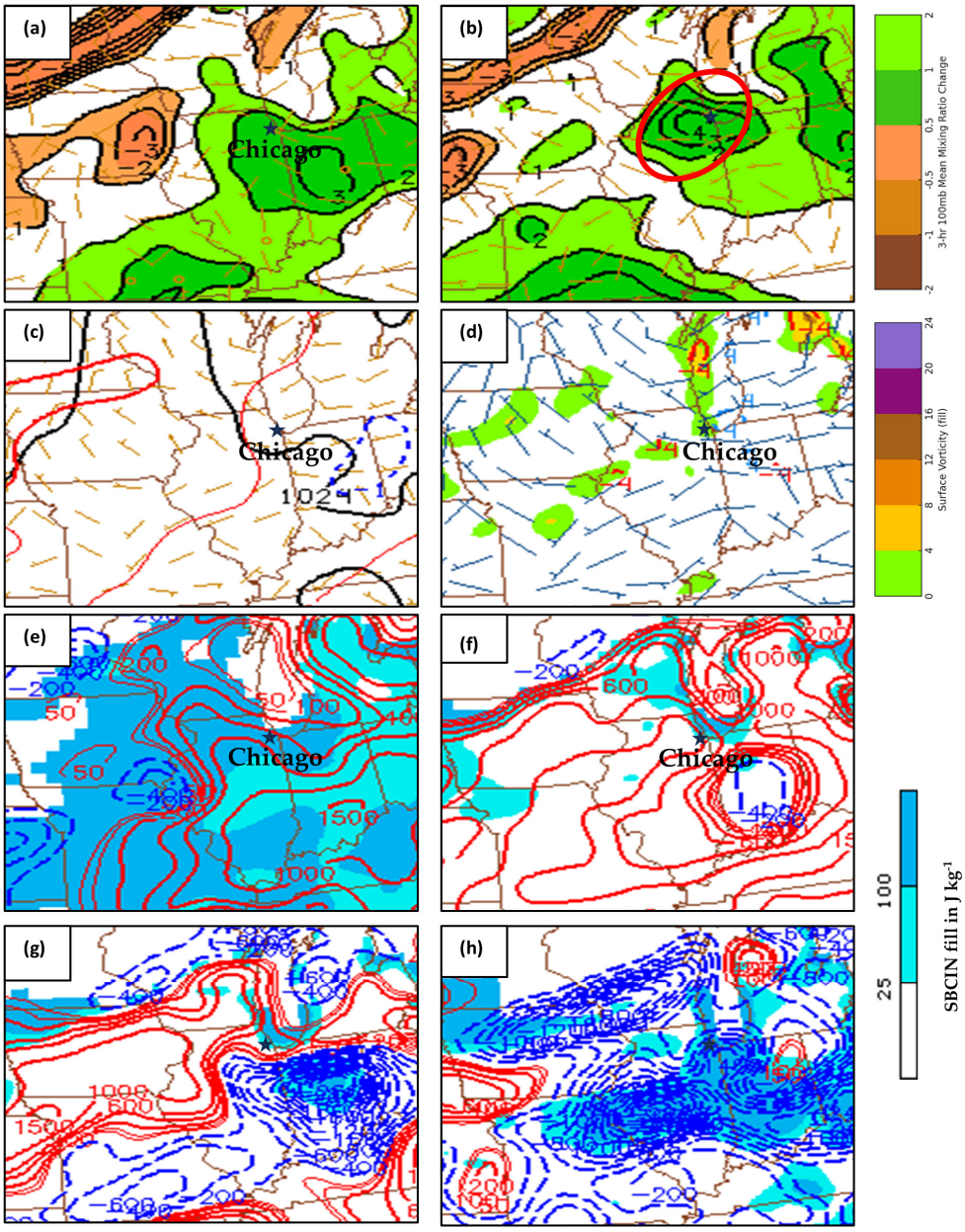


**Figure 10.** Zoomed in area of RUC analysis of the lowest 100 hPa three-hour mean mixing ratio change (color fill, g kg$^{-1}$ [3 h]$^{-1}$) and surface wind barbs (kt) valid at (**a**) 12007/5 and (**b**) 14007/5. (**c**) Pressure (MSLP, black solid, hPa) and MSLP tendency (red solid positive, dashed blue negative, hPa [2 h]$^{-1}$) valid at 16007/5. (**d**) Surface wind barbs (kt), surface vorticity (color fill, $10^{-5}$ s$^{-1}$), and surface divergence (red solid positive, blue dashed negative, $10^{-5}$ s$^{-1}$) valid at 16007/5. RUC analysis of three-hour SBCAPE change (red solid positive, blue dashed negative, J kg$^{-1}$) and SBCIN (blue fill, J kg$^{-1}$) valid at (**e**) 12007/5, (**f**) 16007/5, (**g**) 18007/5, and (**h**) 22007/5. Star indicates location of Chicago, IL, USA. Red oval shape in (**d**) highlights area of maximum mixing ratio change just southeast of Chicago, IL, USA. Black contour in (**c**) just southwest of Chicago indicates the trough.

## 5. Meso-β/γ Scale Convective Evolution

The previously described adjustments have established a highly favorable environment for moist convection over and surrounding Chicago, as exemplified by the Doppler radar-derived features displayed in Figure 12. The surface pressure trough and low-level velocity convergence as well as northwestward-building upper-level velocity divergence force mid-tropospheric ascent combined with very large SBCAPE and MUCAPE (nearly equivalent values) approaching 3000 J kg$^{-1}$ and a low lifted parcel level (LPL) ~1000 m

where parcels realize that potential instability. These features set up the lower-end meso-β and larger-end meso-γ scale environment for moist convection consistent with the following studies [37–39].

The surface meteograms for NWS (KLOT), and three Chicago airports [KMDW, O'Hare (KORD), and Wheeling (KPWK); Figure 11a–d)] indicate the following key signals consistent with the analyses presented in this manuscript in the pre-convective and early convective environments: (1) convection was first observed between 18007/5 and 19007/5 at all Chicago airport locations or observation sites, or within visual distance of these locations, (2) very strong surface heating and cooling spikes occurred during and shortly after the 18007/5–19007/5 period, with the most significant dual spikes at KMDW during and immediately after the time convection arrived, and (3) generally, a shift is observed from north-northwesterly surface flow to south-southeasterly during the pre-convective-post-convective period starting at 1800 UTC and ending at 2100 UTC. Even in the far western suburbs at DuPage County, IL Airport (KDPA) and to the southeast at Gary, IN (KGYY), strong signals of these pressure, wind, and temperature features can be observed in the surface meteograms in Figure 11e,f. KDPA is particularly interesting because very little, if any, rain is observed there, but strong wind, pressure, and temperature changes are observed, indicating the strength of the surface features forced by moist convection.

There are three key time intervals (periods #1–3) that encapsulate the evolution of QLCS#1 and #2 that propagate over the Chicago metroplex, as depicted in Figure 12. The first QLCS evolution is much more complicated than the second system, as will be shown in Figure 12. During 1700–1800 UTC, i.e., period #1, the mesoscale convective system (MCS), which developed over northern Indiana shortly before 1600 UTC, propagated south-southwestwards towards eastern Illinois, shedding smaller MCS until it encountered the persistent surface trough mentioned earlier and depicted in Figure 10c,d that is oriented northwest–southeast through Chicago. That trough is the locus at the meso-β scale of initial convective triggering southwest and northwest of Chicago (note Figure 12a). By 18007/5, two groups of cells developed, one on the southwest side of the city between Joliet and KMDW and one on the northwest side between Hoffman Estates and Aurora, both of which were roughly embedded within the pressure trough mentioned above (Figure 12b).

During period #2, 18007/5–22007/5 in Figure 12b–l, convection intensified in three zones: one on the southwest side of the city between Joliet and KMDW, one on the northwest side of the city between Hoffman Estates and Aurora, and a third over the southeastern side of the city near the lakeshore extending south of the Loop. The third zone developed around 18307/5, and as the short period Doppler sequences show during the 18307/5 through 19157/5 period (Figure 12d–i), all three zones intensified with numerous >50 dBz cells that changed their location very slowly but eventually merged around the city, forming a triangular-shaped radar depiction by 18507/5 (Figure 12g). The bulk of this second period from 1800–2100 UTC then followed a simple evolution, with the entire mass of cells slowly propagating to the southeast along the lakeshore, then filling the internal clear region as they completely merge after moving southeast of the metroplex by 2100 UTC to form a weakening and weakly bowing MCS as can be seen in Figure 12h–k. Prior to weakening during primarily 18307/5–19307/5, the >50 dBz cells fill in the clear zone in the early triangular center and, as will be shown from the Doppler precipitation, produce heavy precipitation from just southeast of KMDW down close to the Indiana border equatorward of the metroplex. It is quite important to note that this triangular radar structure remained intact for ~50 min while transiting the city, then appears to have merged as a slightly comma-shaped convective mass generally after 19007/5 (Figure 12h). It is also important to point out that the embryonic triangular radar structure at ~18307/5 was east of the NWS Romeoville Doppler and southwest of the Loop or roughly just south-southeast of KMDW.

This location is consistent with model simulations and observations of maximum surface temperatures and meso-low/high formation and intensification to be shown in Part II, as well as being closely adjacent to upper-level divergence and low-level convergence, all best simulated by the WRF-UCM. Figures 12h,i and 13c,d confirm the filling in of the highest reflectivity >50 dBz and that the heaviest precipitation accumulation just south-southeast of KMDW extends down to Evergreen Park and Calumet near the Indiana border.

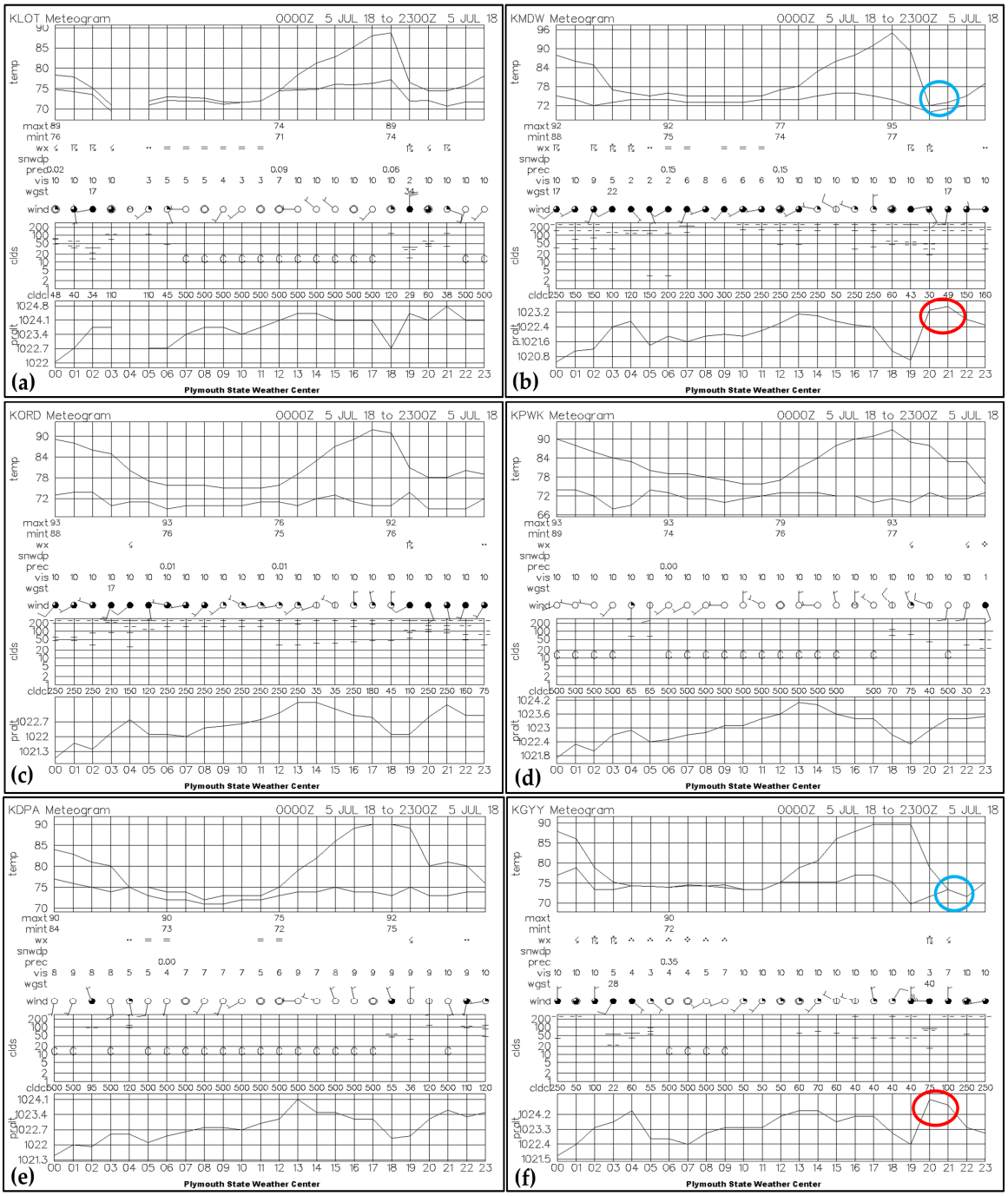


**Figure 11.** Observed Plymouth State Weather Center's surface meteograms at (**a**) Romeoville, Illinois (KLOT), (**b**) Midway Airport (KMDW), (**c**) O'Hare Airport (KORD), (**d**) Wheeling, Illinois (KPWK), (**e**) DuPage County, Illinois (KDPA), and (**f**) Gary, Indiana (KGYY) for period 0000–2300 UTC 5 July 2018. Temperature drop (sky oval shape) and pressure rise (red oval shape) at KMDW (**b**) and KGYY (**f**) between 1900 and 2000 UTC.

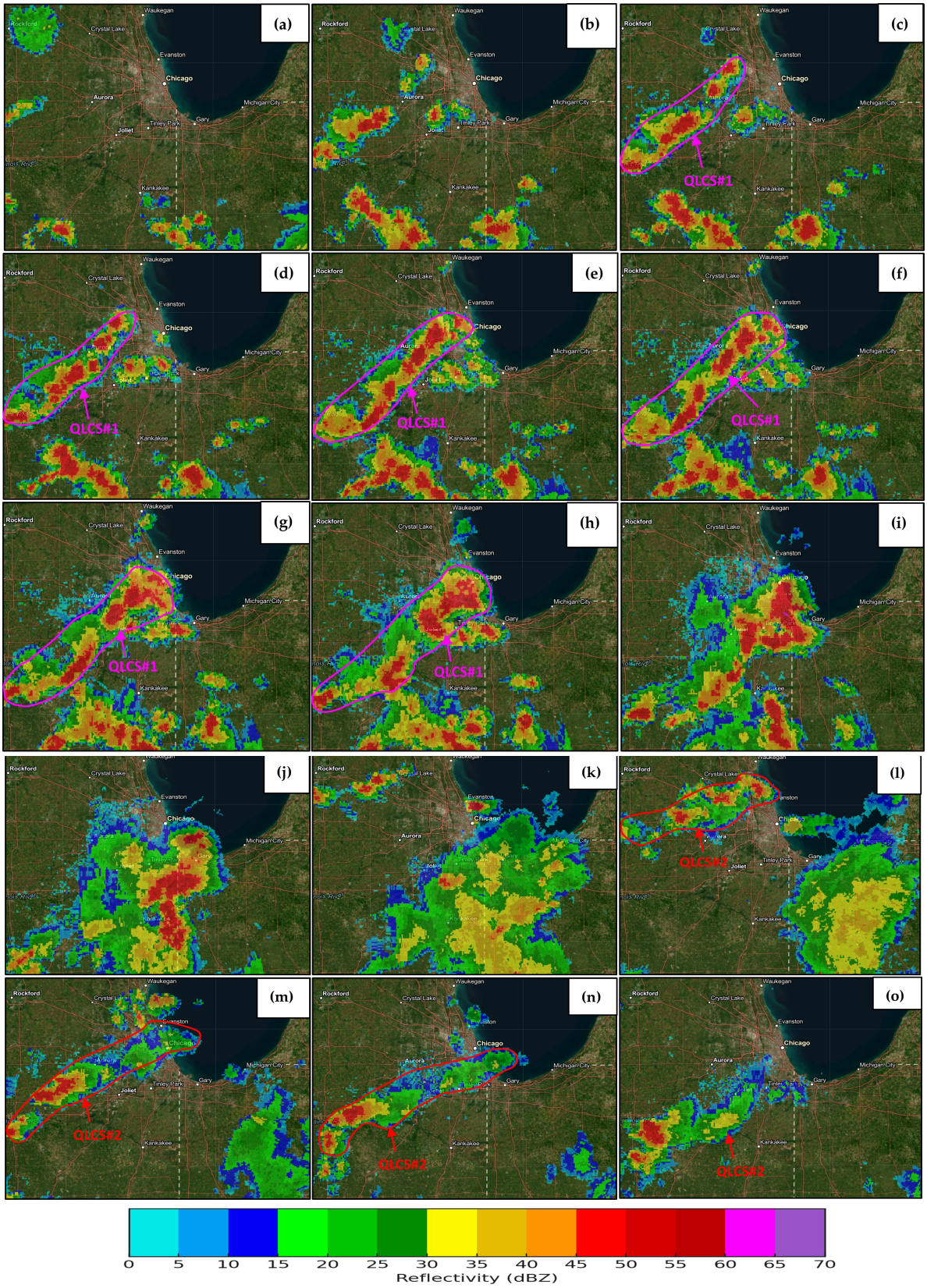


**Figure 12.** NOAA NEXRAD Doppler composite reflectivity (dBz) valid at (**a**) 1700 UTC, (**b**) 1800 UTC, (**c**) 1810 UTC, (**d**) 1820 UTC, (**e**) 1840 UTC, (**f**) 1845 UTC, (**g**) 1855 UTC, (**h**) 1905 UTC, (**i**) 1930 UTC, (**j**) 2000 UTC, (**k**) 2100 UTC, (**l**) 2200 UTC, (**m**) 2300 UTC, (**n**) 2330 UTC 5 July 2018, and (**o**) 0000 UTC 6 July 2018. Purple color annotation indicates evolution of QLCS #1, and red color annotation indicates evolution of QLCS#2.

During period #3, 22007/5-00007/6, the QLCS #1 convection weakened rapidly near and southwest of Gary, IN (KGYY) while QLCS #2 developed around 19307/5 near Rockford, IL (KRFD) and strengthened into an active squall line oriented southwest–northeast about the time the polar front emerges in northeastern Illinois from southeastern Wisconsin as can be seen in Figure 12l–o. However, by the period of 22007/5–23007/5, after achieving the maximum number of 50 dBz cells northwest of Chicago, the QLCS #2 dissipates very rapidly during a period of strengthening upper-level convergence, sinking air, and rapid mid-tropospheric drying above 800 hPa over the region in which the dry air aloft overtakes residual moisture below 900 hPa as indicated in Figures 7a–f and 12m–o.

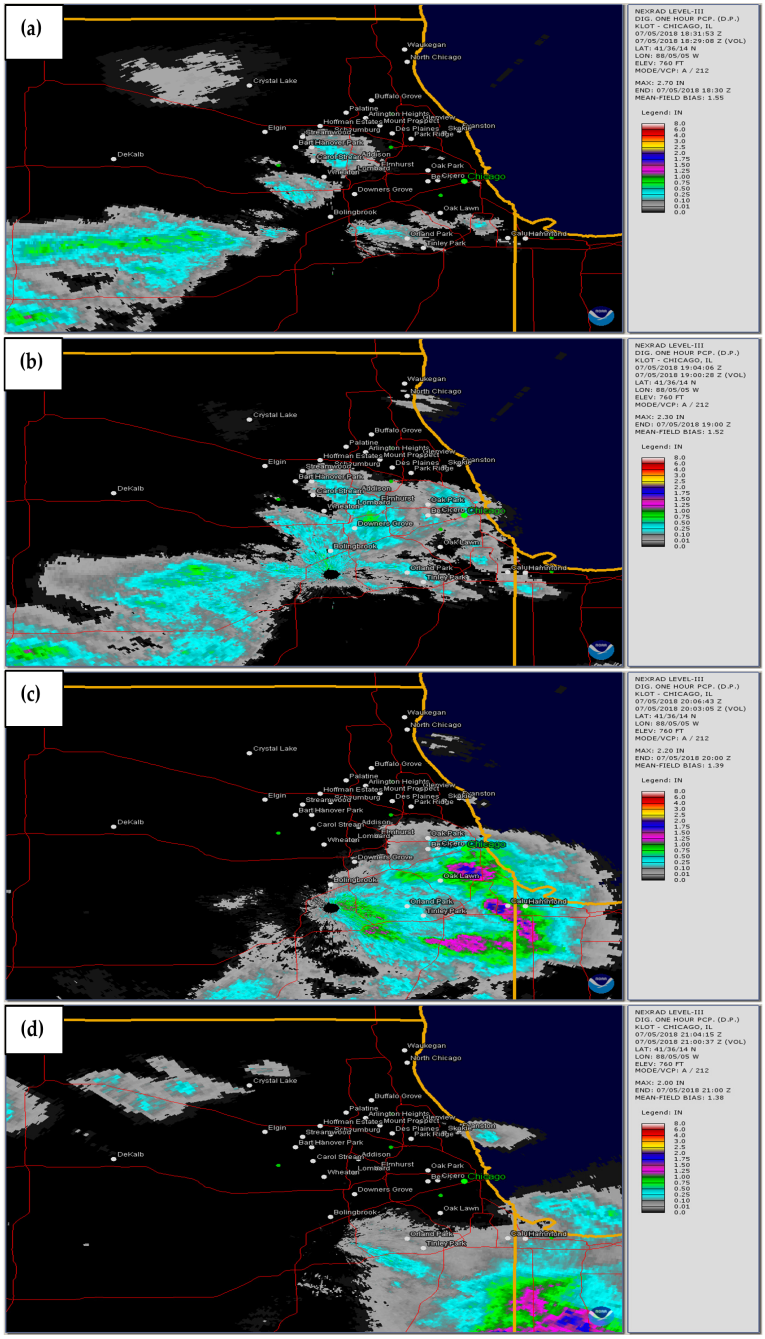


**Figure 13.** *Cont.*

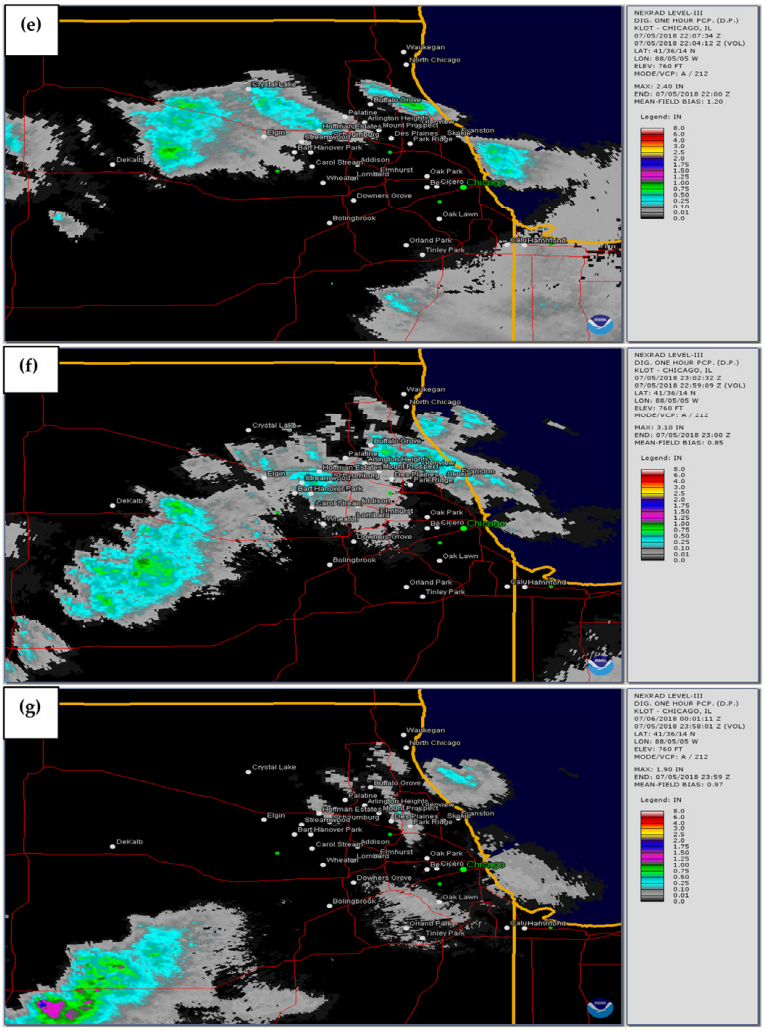


**Figure 13.** NWS Chicago/Romeoville (KLOT) one-hour Doppler-derived rainfall totals (in) valid at approximately (**a**) 18307/5, (**b**) 19007/5, (**c**) 20007/5, (**d**) 21007/5, (**e**) 22007/5, (**f**) 23007/5, (**g**) 00007/6 at KLOT. For this event, precipitation scale for hourly rates in inches roughly ranges from 0.25–0.50 light blue, 0.50–0.75 green, 0.75–1.25 magenta, and 1.25–1.75 dark blue.

Finally, in this subsection, we examine and depict the 60 min Doppler precipitation totals in Figure 13, which indicate (1) the primary QLCS #1 development as noted earlier in the quasi-stationary southwest-northeast trough during 18007/5–19007/5, (2) a separate cell on the southwest side of the city, indicating a restructuring of that QLCS by an isolated updraft or possibly by the city during 1830–19007/5, (3) and the dramatic increase of precipitation rate during 1900–20007/5 roughly over the region near and southeast of KMDW in between the converging cells' reflectivity patterns in Figure 12h–j. It should be noted that the meteogram totals for the final 6 h of 5 July 2018 depicted on the 00007/6 diagram indicate that KMDW had the most precipitation of all four Chicago locations, including Romeoville of ~0.52 in.; however, that total is substantially less than the Doppler estimate in Figure 13c just southeast of that location indicating peak total precipitation accumulation exceeding 1 inch during 1830–2000 UTC. After moving over the southern side of the city into northwestern Indiana, QLCS#1 produced significant precipitation. However, following this time, QLCS#2 only produced significant precipitation poleward and along the lakeshore of Chicago. It rapidly dissipated over the city, as can be seen in the Doppler sequence in Figure 13e–g.

## 6. Summary and Conclusions

The multi-scale observations indicate that an expansive ridge of high pressure aloft elongates across much of the U.S. with an area of weak diffluence on its northwestern flank setting up over Chicago, IL, USA, and its adjacent cities. Substantial moisture transport around the ridge at low-levels in conjunction with a slow-moving surface trough creates a favorable convective scenario at the meso-$\alpha/\beta$ scale east and equatorward of the city, generating very large SBCAPE values. The upper-tropospheric divergence within the diffluent side of the ridge is strengthened by the outflow from early moist convection, which builds poleward and westward in time, propagating over and strengthening the weak surface trough. A line of convection within the trough builds northeastwards through the city, with cells triggering on the southwest, northwest, and southeastern flanks roughly centered on Midway Airport and its environs. The structure of the convection surrounds the downtown region roughly centered near KMDW and fills in and strengthens in time. Cold outflow builds a meso-high that propagates poleward through Chicago, rotating the surface winds nearly 180 degrees towards the north. The observations indicate that after intensifying and building northwestwards through Chicago from the southeast, the first QLCS then propagated southeastwards into northern Indiana after producing heavy precipitation near and south-southeast of KMDW, with the second QLCS developing roughly in between the outflow moving poleward from the QLCS#1 meso-high and an approaching polar cold front over northern Illinois. The second QLCS dissipated rapidly over the city as it encountered the residual cold pool, as well as overtaking dry air aloft, descent, and low-level divergence over the metroplex.

In Part II, we will assess the role of the urban heat island as simulated by both WRF-ARW and WRF-UCM in organizing the instability and convergence necessary for the organization and evolution of these QLCS and how the urban canopy improves the simulation of convective evolution.

**Author Contributions:** Conceptualization, M.L.K.; methodology, M.L.K. and S.M.S.K.; software: S.M.S.K.; validation, M.L.K. and S.M.S.K.; formal analysis, M.L.K. and S.M.S.K.; investigation, M.L.K. and S.M.S.K., resources, M.L.K. and Y.-L.L.; data curation, M.L.K. and S.M.S.K.; writing—original draft presentation, M.L.K.; writing—review and editing, M.L.K., S.M.S.K. and Y.-L.L.; visualization, S.M.S.K.; supervision, M.L.K. and Y.-L.L.; project administration, M.L.K. and Y.-L.L.; and funding acquisition, M.L.K. and Y.-L.L. All authors have read and agreed to the published version of the manuscript.

**Funding:** This research was funded by the Department of Energy under contract # DE-SC0023240.

**Institutional Review Board Statement:** Not applicable.

**Informed Consent Statement:** Not applicable.

**Data Availability Statement:** The datasets generated during and/or analyzed during the current study are available from the second author upon reasonable request. The data are not publicly available due to privacy.

**Acknowledgments:** The authors would like to acknowledge NCAR and the Computational and Information Systems Laboratory (CISL) for their support of computing times on the Cheyenne supercomputer (Project No. UNCT0001 and UNCT0005). The comments from anonymous reviewers, which helped to improve the quality of the paper, are highly appreciated.

**Conflicts of Interest:** The authors declare no conflicts of interest. The funders had no role in the design of the study; in the collection, analyses, or interpretation of the data; in the writing of the manuscript; or in the decision to publish the results.

## Abbreviations

The following abbreviations are used in this manuscript:

| | |
|---|---|
| QLCS | quasi-linear convective system |
| UHI | urban heat island |
| URI | urban river island |
| RUC | Rapid Update Cycle |
| PV | potential vorticity |
| WRF-ARW | Weather Research and Forecasting–Advanced Research Weather Model |
| WRF-UCM | Weather Research and Forecasting–Urban Canopy Model |
| CAPE | convective available potential energy |
| SBCAPE | surface-based convective available potential energy |
| MUCAPE | most unstable convective available potential energy |
| MLCAPE | mixed-layer convective available potential energy |
| PBL | planetary boundary layer |
| LCL | lifting condensation level |
| CIN | convective inhibition |
| SBCIN | surface-based convective inhibition |
| AGL | above ground level |
| MSLP | mean sea level pressure |
| KMDW | Midway Airport, Chicago |
| KORD | O'Hare Airport, Chicago |
| KPWK | Wheeling Airport, Chicago |
| KLOT | Lewis University Airport, Chicago/Romeoville |
| KDPA | DuPage Airport |
| KGYY | Gary, Indiana |
| LPL | lifted parcel level |
| MCS | mesoscale convective system |

## References

1. Huff, F.A.; Urban, J.L.V. Topographic and Diurnal Effects on Rainfall in the St. Louis Region. *J. Appl. Meteorol. Climatol.* **1978**, *17*, 565–577. [CrossRef]
2. Changnon, S.A. Rainfall Changes in Summer Caused by St. Louis. *Science* **1979**, *205*, 402–404. [CrossRef] [PubMed]
3. Braham, R.R.; Semonin, R.G.; Auer, A.H.; Changnon, S.A.; Hales, J.M. Summary of Urban Effects on Clouds and Rain. In *Metromex: A Review and Summary. Meteorological Monograph*; Changnon, S.A., Ed.; American Meteorology Society: Boston, MA, USA, 1981; Volume 18, pp. 141–152.
4. Changnon, S.A.; Huff, F.A.; Semonin, R.G. METROMEX: An investigation of inadvertent weather modification. *Bull. Am. Meteorol. Soc.* **1971**, *52*, 958–968. [CrossRef]
5. Changnon, S.A.; Huff, F.A.; Schickedanz, P.T.; Vogel, J.L. *Summary of METROMEX, Volume 1: Weather Anomalies and Impacts*; Bulletin 62; Illinois State Water Survey: Urbana, IL, USA, 1977.
6. Bentley, M.L.; Stallins, J.A.; Ashley, W.S. Synoptic environments favourable for urban convection in Atlanta, Georgia. *Int. J. Climatol.* **2012**, *32*, 1287–1294. [CrossRef]
7. Bornstein, R.; Lin, Q. Urban heat islands and summertime convective thunderstorms in Atlanta: Three case studies. *Atmos. Environ.* **2000**, *34*, 507–516. [CrossRef]
8. Shepherd, J.M.; Pierce, H.; Negri, A.J. Rainfall Modification by Major Urban Areas: Observations from Spaceborne Rain Radar on the TRMM Satellite. *J. Appl. Meteorol.* **2002**, *41*, 689–701. [CrossRef]
9. Seto, K.C.; Shepherd, J.M. Global urban land-use trends and climate impacts. *Curr. Opin. Environ. Sustain.* **2009**, *1*, 89–95. [CrossRef]
10. Han, J.-Y.; Baik, J.-J.; Lee, H. Urban impacts on precipitation. *Asia-Pac. J. Atmos. Sci.* **2014**, *50*, 17–30. [CrossRef]
11. Liu, J.; Niyogi, D. Meta-analysis of urbanization impact on rainfall modification. *Sci. Rep.* **2019**, *9*, 7301. [CrossRef]
12. Shen, Y.; Yang, L. Divergent Urban Signatures in Rainfall Anomalies Explained by Pre-Storm Environment Contrast. *Geophys. Res. Lett.* **2023**, *50*, e2022GL101658. [CrossRef]

13. Bornstein, R.D. Observations of the Urban Heat Island Effect in New York City. *J. Appl. Meteorol. Climatol.* **1968**, *7*, 575–582. [CrossRef]
14. Dixon, P.G.; Mote, T.L. Patterns and Causes of Atlanta's Urban Heat Island–Initiated Precipitation. *J. Appl. Meteorol.* **2003**, *42*, 1273–1284. [CrossRef]
15. Miao, S.; Chen, F.; LeMone, M.A.; Tewari, M.; Li, Q.; Wang, Y. An Observational and Modeling Study of Characteristics of Urban Heat Island and Boundary Layer Structures in Beijing. *J. Appl. Meteorol. Climatol.* **2009**, *48*, 484–501. [CrossRef]
16. Yang, L.; Tian, F.; Smith, J.A.; Hu, H. Urban signatures in the spatial clustering of summer heavy rainfall events over the Beijing metropolitan region. *J. Geophys. Res. Atmos.* **2014**, *119*, 1203–1217. [CrossRef]
17. Li, W.; Zhao, M.; Scaoini, M.; Hosseini, S.; Wang, X.; Yao, D.; Zhang, K.; Gao, J.; Li, X. Extreme rainfall trends of 21 typical urban areas in China during 1998–2015 based on remotely sensed data sets. *Environ. Monit. Assess.* **2019**, *191*, 709. [CrossRef]
18. Sun, X.; Luo, Y.; Gao, X.; Wu, M.; Li, M.; Huang, L.; Zhang, D.-L.; Xu, H. On the Localized Extreme Rainfall over the Great Bay Area in South China with Complex Topography and Strong UHI Effects. *Mon. Weather Rev.* **2021**, *149*, 2777–2801. [CrossRef]
19. Han, L.; Wang, L.; Chen, H.; Xu, Y.; Sun, F.; Reed, K.; Deng, X.; Li, W. Impacts of Long-Term Urbanization on Summer Rainfall Climatology in Yangtze River Delta Agglomeration of China. *Geophys. Res. Lett.* **2022**, *49*, e2021GL097546. [CrossRef]
20. Steensen, B.M.; Marelle, L.; Hodnebrog, Ø.; Myhre, G. Future urban heat island influence on precipitation. *Clim. Dyn.* **2022**, *58*, 3393–3403. [CrossRef]
21. Miao, S.; Chen, F.; Li, Q.; Fan, S. Impacts of Urban Processes and Urbanization on Summer Precipitation: A Case Study of Heavy Rainfall in Beijing on 1 August 2006. *J. Appl. Meteorol. Climatol.* **2011**, *50*, 806–825. [CrossRef]
22. Niyogi, D.; Pyle, P.; Lei, M.; Arya, S.P.; Kishtawal, C.M.; Shepherd, M.; Chen, F.; Wolfe, B. Urban Modification of Thunderstorms: An Observational Storm Climatology and Model Case Study for the Indianapolis Urban Region. *J. Appl. Meteorol. Climatol.* **2011**, *50*, 1129–1144. [CrossRef]
23. Yang, L.F.; Li, Q.; Yuan, H.; Niu, Z.; Wang, L. Impacts of Urban Canopy on Two Convective Storms with Contrasting Synoptic Conditions Over Nanjing, China. *J. Geophys. Res. Atmos.* **2021**, *126*, e2020JD034509. [CrossRef]
24. Rosenfeld, D.; Lohmann, U.; Raga, G.B.; O'Dowd, C.D.; Kulmala, M.; Fuzzi, S.; Reissell, A.; Andreae, M.O. Flood or Drought: How Do Aerosols Affect Precipitation? *Science* **2008**, *321*, 1309–1313. [CrossRef] [PubMed]
25. Hosannah, N.; Gonzalez, J.E. Impacts of Aerosol Particle Size Distribution and Land Cover Land Use on Precipitation in a Coastal Urban Environment Using a Cloud-Resolving Mesoscale Model. *Adv. Meteorol.* **2014**, *2014*, 904571. [CrossRef]
26. Zhong, S.; Qian, Y.; Zhao, C.; Leung, R.; Yang, X.-Q. A case study of urbanization impact on summer precipitation in the Greater Beijing Metropolitan Area: Urban heat island versus aerosol effects. *J. Geophys. Res. Atmos.* **2015**, *120*, 903–914. [CrossRef]
27. Zhang, X.; Yang, Y.; Chen, B.; Huang, W. Operational Precipitation Forecast over China Using the Weather Research and Forecasting (WRF) Model at a Gray-Zone Resolution: Impact of Convection Parameterization. *Weather Forecast.* **2021**, *36*, 915–928. [CrossRef]
28. Niyogi, D.; Pyle, P.; Lei, M.; Kishtawal, C.; Schmid, P.; Shepherd, M. Urbanization Impacts on the Summer Heavy Rainfall Climatology over the Eastern United States. *Earth Interact.* **2017**, *21*, 1–17. [CrossRef]
29. Qian, Y.; Chakraborty, T.C.; Li, J.; Li, D.; He, C.; Sarangi, C.; Chen, F.; Yang, X.; Leung, L.R. Urbanization Impact on Regional Climate and Extreme Weather: Current Understanding, Uncertainties; Future Research Directions. *Adv. Atmos. Sci.* **2022**, *39*, 819–860. [CrossRef]
30. Keeler, J.M.; Kristovich, D.A.R. Observations of Urban Heat Island Influence on Lake-Breeze Frontal Movement. *J. Appl. Meteorol. Climatol.* **2012**, *51*, 702–710. [CrossRef]
31. Jiang, P.; Wen, Z.; Sha, W.; Chen, G. Interaction between turbulent flow and sea breeze front over urban-like coast in large-eddy simulation. *J. Geophys. Res. Atmos.* **2017**, *122*, 5298–5315. [CrossRef]
32. NOAA SPC. SPC Hourly Mesoscale Analysis Data, Archive National Sector (s4). Available online: https://www.spc.noaa.gov/exper/ma_archive/ (accessed on 5 April 2024).
33. UWYO. University of Wyoming Archive Sounding Data. Available online: https://weather.uwyo.edu/upperair/sounding.html (accessed on 5 April 2024).
34. Plymouth SWC. Plymouth State Weather Center Data Archive. Available online: https://vortex.plymouth.edu/myowxp/sfc/statlog-a.html (accessed on 5 April 2024).
35. NOAA NEXRAD. NOAA National Weather Service (NWS) Radar Operations Center (1992): NOAA Next Generation Radar (NEXRAD) Level 3 Products. [Precipitation]. NOAA National Centers for Environmental Information. NCEI DSI 7000. Available online: https://www.ncei.noaa.gov/maps/radar/ (accessed on 5 April 2024).
36. Hamilton, D.W.; Lin, Y.L.; Weglarz, R.P.; Kaplan, M.L. Jetlet formation from diabatic forcing with applications to the 1994 Palm Sunday tornado outbreak. *Mon. Weather Rev.* **1998**, *126*, 2061–2089. [CrossRef]
37. Kaplan, M.L.; Zack, J.W.; Wong, V.C.; Tuccillo, J.J. Initial results from a Mesoscale Atmospheric Simulation System and comparisons with the AVE-SESAME I data set. *Mon. Weather Rev.* **1982**, *110*, 1564–1590. [CrossRef]

38. Kaplan, M.L.; Lin, Y.-L.; Hamilton, D.W.; Rozumalski, R.A. The numerical simulation of an unbalanced jetlet and its role in the Palm Sunday 1994 tornado outbreak in Alabama and Georgia. *Mon. Weather Rev.* **1998**, *126*, 2133–2165. [CrossRef]
39. Maddox, R.A.; Perkey, D.J.; Fritsch, J.M. Evolution of upper tropospheric features during the development of a mesoscale convective complex. *J. Atmos. Sci.* **1981**, *38*, 1664–1674. [CrossRef]